



Cite this: *Mater. Adv.*, 2023, 4, 504

Alkoxy phosphonic acid-functionalized conjugated microporous polymers for efficient and multi-environmental proton conduction†

Kaijie Yang,^a Yuxiang Wang,^a Zhiyi Ling,^a Xiaogang Pan,^b Gen Zhang  ^{*a} and Jian Su  ^{*ac}

Proton-conducting materials are key components of proton exchange membrane fuel cells that can convert chemical fuel into electrical energy directly, efficiently, and without pollution. Despite the creation of various proton-conducting polyelectrolytes over the past decade, there is still a lack of robust electrolytes that can simultaneously satisfy high proton conductivity and multi-environmental conditions. Herein, we designed and synthesized a series of alkoxy phosphonic acid-functionalized conjugated microporous polymers (CMPs) through side-chain engineering and Sonogashira–Hagihara cross coupling. With superior stability, hydrophilic nature and high side-chain mobility, the phosphonated CMPs further serve as robust hosts to accommodate a large number of H_3PO_4 molecules through hydrogen-bonding, and exhibit high proton conductivity in pelletized powder samples under multi-environment conditions, such as wide temperature range anhydrous proton conductivities of 2.15×10^{-2} and $1.15 \times 10^{-5} \text{ S cm}^{-1}$ at 130 and -40°C , respectively, and a wide humidity range proton conductivity of 1.87×10^{-2} and $9.93 \times 10^{-2} \text{ S cm}^{-1}$ at 30°C under 32% relative humidity and 90°C under 98% relative humidity, respectively. To the best of our knowledge, this is the first example of constructing multi-environmentally adaptable porous organic polymer proton-conducting materials for both humid and anhydrous conditions within a wide temperature range (-40 to 130°C).

Received 19th September 2022,
Accepted 9th November 2022

DOI: 10.1039/d2ma00909a

rsc.li/materials-advances

Introduction

As the core component of proton exchange membrane fuel cells (PEMFCs), proton conducting materials play a vital role in the realization of green and advanced energy conversion. Typically, proton conduction can be divided into water-mediated, that is, proton conduction under relative humidity (RH), and anhydrous proton conduction. Commercially available NafionTM has been able to achieve efficient proton conduction (10^{-2} to $10^{-1} \text{ S cm}^{-1}$) under a high relative humidity (98% RH).^{1–5} The disadvantage, however, is that proton conduction with the maximum effect can only be achieved in a narrow range of operating temperature below 80°C . At a higher operating

temperature, it is always accompanied by the leakage of inner water medium and other guests, which leads to significantly lower proton conductivity, higher cost, and insufficient lifetime.^{1,6–10} Similarly, serious damage to the hydrated PEMs will be induced by freeze/thaw cycles on operation below -5°C .¹¹ For anhydrous proton conduction, operating above 100°C has the advantage of fast kinetics.^{1,12–14} In the meantime, on-board fuel cells not only require high proton conductivity at medium and high temperatures, but also require appropriate functioning for start-up at room temperature, even in subzero climates, such as in high-altitude drones.^{11,15,16} Therefore, designing universal proton-conducting materials that can perform well over a wide temperature range including at subzero temperatures, and that are versatile under both humid and anhydrous conditions, is a matter of great urgency.^{17–19}

In recent years, porous materials such as metal-organic frameworks (MOFs),^{20–23} covalent organic frameworks (COFs),^{24–26} hydrogen-bonded organic frameworks (HOFs),²⁷ and porous organic polymers (POPs),^{28–30} shown to possess flexibly functionalized frameworks together with concurrent control of pore size, shape, and interface, have gradually been branching out into the field, whether as a support for humid proton conduction or for anhydrous proton conduction. Conjugated microporous

^a Key Laboratory for Soft Chemistry and Functional Materials of Ministry of Education, School of Chemistry and Chemical Engineering, Nanjing University of Science and Technology, Nanjing, Jiangsu 210094, China

E-mail: sujian@njust.edu.cn, zhanggen@njust.edu.cn

^b School of Electrical Engineering, Southeast University, Nanjing, Jiangsu 210096, China

^c State Key Laboratory of Coordination Chemistry, Nanjing University, Nanjing, Jiangsu 210023, China

† Electronic supplementary information (ESI) available. See DOI: <https://doi.org/10.1039/d2ma00909a>



polymers (CMPs), due to their synthetic simplicity, solid structure, and tunable porosity, have attracted much attention and been applied in various fields, such as gas storage and separation,^{31,32} adsorption and encapsulation of chemicals,^{33,34} heterogeneous catalysis,^{35,36} photoredox catalysis,^{37,38} light emittance,^{39,40} and so on. So far, for proton conduction, among POPs doped with an additional proton source such as acid, their highest humid and anhydrous proton conductivities are revealed as $\sim 10^{-1}$ S cm⁻¹ for SPAF-1 and $\sim 10^{-3}$ S cm⁻¹ for H₃PO₄@CMP-F6-60%, respectively.^{27,28,30,41-45} For operation above 80 °C and below -5 °C, the research and development of guest-induced anhydrous proton-conductors is the top priority. Thus far, PA@TpBpy-MC and H₃PO₄@TPB-DMeTP-COF have been reported to achieve high anhydrous proton conductivities of $\sim 10^{-4}$ and $\sim 10^{-1}$ S cm⁻¹ at -40 °C and 160 °C, respectively.^{18,25} Under humid conditions, the proton conductivities of some composite membranes have reached up to 10⁻¹ S cm⁻¹.⁴⁶⁻⁴⁸ However, there are rare reports on conductive materials with high efficiency that simultaneously achieve applications under humid and anhydrous conditions. In the reported works, PA@Tp-Azo exhibits an anhydrous proton conductivity of 9.9×10^{-4} S cm⁻¹ at 67 °C and a humid proton conductivity of 6.70×10^{-5} S cm⁻¹ at 59 °C under 98% RH, and MPOPS-1 displays proton conductivities of 1.49×10^{-5} and 3.07×10^{-2} S cm⁻¹ at 77 °C under anhydrous and humid conditions, respectively.^{30,49} Notably, there is no further report on novel universal proton-conducting materials that are applicable to a wide temperature range under both humid and anhydrous conditions.

Typically, phosphoric acid is extensively used as a proton carrier due to its high dissociation constant, and non-volatile, and non-toxic properties.⁵⁰ However, avoiding the leaching of phosphoric acid under humid conditions and maintaining its efficient proton transfer in a wide temperature range are the real problems to be solved. Herein, we successfully synthesized a series of hydrophilic phosphonic acid group-functionalized CMPs. The phosphonated CMP frameworks show satisfactory acid resistance and thermal stability, and exhibit high porosity. Upon doping with H₃PO₄, the composited CMPs, denoted as **CMP-P-H** and **CMP-Cx-P-H**, reveal stable and efficient proton conduction under complex harsh conditions, including anhydrous 130 and -40 °C, and high humidity (98% RH) 90 °C. The fast proton transfer is mainly attributed to the multi-point triggered formation of hydrogen-bonding interactions between the phosphonic acid groups anchored within CMP frameworks and the doped guest H₃PO₄ molecules. The hydrogen-bonding interactions have been illustrated using the XPS and FT-IR spectra.

Experimental

Materials and methods

All the chemicals and solvents used in the syntheses were commercially purchased and of reagent grade, and can be used without further purification. 2,5-Dibromohydroquinone and 1,3,5-triethynylbenzene were purchased from Heowns Biotech

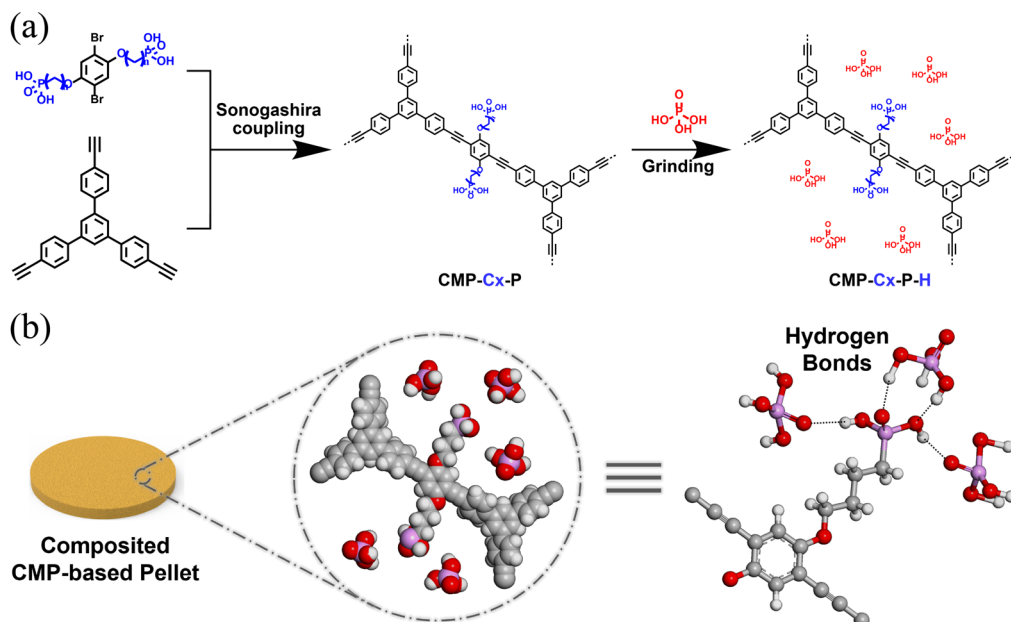
LLC (Tianjin, China). 1,2-Dibromoethane, 1,4-dibromobutane and 1,6-dibromohexane were purchased from Dibo Biotech Co., Ltd (Shanghai, China). Triethyl phosphite and Pd(PPh₃)₂Cl₂ were purchased from Wanqing Chemical Glassware Instrument Co., Ltd (Nanjing, China). All the solvents such as acetonitrile, triethylamine, dichloromethane, acetone, methanol, and *N,N*-dimethylformamide were purchased from Sinopharm (Beijing, China).

All samples were characterized and analyzed according to conventional techniques. Powder X-ray diffraction (PXRD) patterns were collected on a Bruker D8 Advance diffractometer using Cu K α radiation. Fourier transform infrared (FT-IR) spectra were obtained on a Thermo Fisher Scientific Optics NICOLETIS10 FT-IR spectrometer with a Universal ATR accessory within the range of 4000 to 500 cm⁻¹. Liquid-state ¹H nuclear magnetic resonance (NMR) spectra were obtained on a Bruker Advance III instrument with a AS500 magnet equipped with a cryoprobe (500 MHz). Liquid-state ¹³C nuclear magnetic resonance spectra were obtained on a Bruker Advance III instrument with a AS500 magnet equipped with a cryoprobe (125 MHz). Liquid-state ³¹P nuclear magnetic resonance spectra were obtained on a Bruker Advance III instrument with a AS500 magnet equipped with a cryoprobe (202.41 MHz). Solid-state ¹³C cross-polarization magic-angle-spinning (CP/MAS) NMR spectra were recorded on a JEOL JNM-ECA 400 MHz, 4.0 mm rotor, MAS of 10 kHz, and recycle delay of 1 s. High-resolution mass spectrometry (HRMS) mass spectra were obtained on a Baird Acquity UPLC/XEVO G2-XS QTOF using CHCl₃ as a solvent. Scanning electron microscopy (SEM) images were collected using a JSM-IT500HR system. Transmission electron microscopy (TEM) images were collected using a JEM-2100, JEOL. Thermogravimetric analysis (TGA) was performed using a NETZSCH STA 449F5 under flowing N₂ (60 mL min⁻¹) with a 10 K min⁻¹ ramp rate. Samples were heated in a platinum pan from 50 °C to 900 °C (10 °C min⁻¹). N₂ adsorption and desorption measurements were performed at 77 K using BEL (MicrotracBEL Corp, Japan), and before the gas adsorption measurements, all the solids were dried at 80 °C under vacuum in a drying oven for 24 h to remove the residual solvent, then all the samples were degassed under vacuum at 100 °C with BELPREP VAC III for 12 h to afford the sample for sorption analysis. The pore size distributions of the samples in this work were estimated using Nonlocal Density Functional Theory (NLDFT) based on the model of N₂/77 K on graphitic carbon with slit pores and the method of Tikhonov regularization. Water vapor adsorption and desorption measurements were performed at 298 K using BEL (MicrotracBEL Corp, Japan). The water contact angles (WACs) were measured on a goniometer (JC2000C, Japan) equipped with video capture. X-Ray photoelectron spectroscopy (XPS) spectra were recorded with a kratos axis supra™ of Shimadzu.

Synthesis of CMPs

A series of phosphonic acid group-functionalized CMPs were synthesized by Sonogashira-Hagihara cross coupling of 1,3,5-triethynyltriphenylbenzene with different phosphonic





Scheme 1 (a) Illustration of the synthesis of the phosphonated CMPs composites with H₃PO₄. (b) Demonstrating the assembly of hydrogen-bonding networks. Pink, P; red, O; white, H; grey, C.

acid group anchored monomers of different lengths. The corresponding CMPs were named **CMP-P** and **CMP-Cx-P** ($x = 2, 4$, and 6 , depending on the number of C atoms in the alkoxy phosphonic acid group side chain; **P** stands for phosphonic acid groups), respectively (Scheme 1a). Note that there is no alkoxy chain between the framework of **CMP-P** and the phosphonic acid groups. Monomer **S3/6/9/12** (0.50 mmol), 1,3,5-triethynyltriphenylbenzene (0.33 mmol), CuI (0.04 mmol) and Pd(PPh₃)₄ (0.02 mmol) were added into NET_3/DMF (1:1, v:v), respectively. The mixture was stirred for 60 h at 80 °C under an argon atmosphere and was allowed to cool to room temperature. The crude was washed with water, methanol, dichloromethane and acetone. Then soxhlet extraction from methanol for 48 h was carried out to ensure there was no unreacted monomer, soaked in dry acetone for 12 h and dried at 80 °C under vacuum for 12 h to give **CMP-P** and **CMP-Cx-P** as yellow powders. Furthermore, **CMP-C2S-P** with smaller pores was also obtained by Sonogashira–Hagihara cross coupling of 1,3,5-triethynylbenzene with monomer **S3** (see the ESI†). **CMP-U**, the unfunctionalized parent CMP without the alkoxy phosphonic acid group side chains, was prepared by Sonogashira–Hagihara cross coupling of 1,3,5-triethynyltriphenylbenzene with 1,4-dibromobenzene (see the ESI†).

Synthesis of H₃PO₄ doped CMPs

Doping non-volatile liquid acids into porous materials is a promising solution for constructing proton-conducting electrolytes, and neat phosphoric acid is the most ideal proton carrier due to its high dissociation constant, non-volatile and green properties. Firstly, the dried powder samples of **CMP-P** and **CMP-Cx-P** (20 mg) were weighed into an agate mortar. Then we doped different amounts of H₃PO₄ into the above mortar.

After smooth manual grinding in a mortar with a pestle, the solids were collected and dried at 100 °C under vacuum for 12 h. The H₃PO₄ doped samples were denoted as **CMP-P-H** and **CMP-Cx-P-H** (**H** represents the percentage of doped H₃PO₄ in the total mass), respectively (Scheme 1a). **CMP-C2S-P-H** and **CMP-U-H** were prepared in the same way.

Proton conductivity measurements

For anhydrous proton conduction, first, the pre-dry CMP powders and H₃PO₄ doped CMP powders were compressed using a powder tabletting machine in the glove box under an argon atmosphere with O₂ and H₂O less than 0.01 ppm at a pressure of 0.2 MPa for about 30 minutes to obtain composite CMP-based electrolyte cylindrical pellets with a diameter of 5 mm. Then, the above pellets were sandwiched between two stainless steel electrodes, respectively, assembling into coin cells. The operating temperatures were controlled by one oven. Alternating-current (AC) impedance spectroscopy measurements were performed using a Solartron1296A electrochemistry workstation over a frequency range of 1 to 1 MHz and a temperature range of –40 to 130 °C. For humid proton conduction, CMP powders and H₃PO₄ doped CMP powders were pressed into cylindrical pellets with a diameter of 5 mm at a pressure of 0.2 MPa for about 30 minutes. These pellets were sandwiched between two platinum electrodes, and then were encapsulated in a glass bottle with a certain relative humidity, which was controlled by a different saturated salt solution. The measurements were similar to those of anhydrous proton conduction, except that the operating temperature range was changed to 30–90 °C.

The proton conductivities were calculated by the equation:

$$\sigma = L/(S \times R)$$



where σ (S cm^{-1}) is the ionic conductivity, L (cm) is the thickness of the electrolyte pellet, S (cm^2) is the area of the electrode, and R (Ω) is the resistance value that can be directly obtained from the profiles in the recorded AC impedance spectra.

The activation energy is further calculated by a linear fit of the Arrhenius equation:

$$\ln(\sigma T) = \frac{-E_a}{kT} + \ln A$$

where E_a (eV) is the transport activation energy, k is the Boltzmann constant, T (K) is the temperature, and A is a pre-exponential factor.

Results and discussion

Characterization of **CMP-Cx-P**

A series of stable phosphonic acid group-functionalized CMPs were obtained *via* Sonogashira–Hagihara cross coupling of 1,3,5-triethynyltriphenylbenzene with four phosphonic acid group anchored monomers of different lengths and named as **CMP-P** and **CMP-Cx-P** ($x = 2, 4$, and 6 ; **P** stands for phosphonic acid groups), respectively. The successful polymerization reaction and the formation of CMPs could be proved by the following experiments.

First, the formation of yellow insoluble solids roughly indicates the polymer state of the products. Second, powder X-ray diffraction (PXRD) measurements show that the diffraction peaks of monomer **S3** and 1,3,5-triethynyltriphenylbenzene disappear in the as-prepared CMPs (Fig. S1, ESI[†]). This phenomenon indicates the disordered structure of **CMP-C2-P**.⁵¹ Third, the results of Fourier transform infrared (FT-IR) spectra (Fig. S2–S4, ESI[†]) also confirm the successful preparation of **CMP-Cx-P** and **CMP-P**. In Fig. S2 (ESI[†]), monomer **S3** shows strong peaks at 3265 cm^{-1} and 537 cm^{-1} , which correspond to the stretching vibrational band of terminal alkynes $-\text{C}\equiv\text{C}-\text{H}$ and $\text{C}-\text{Br}$, while a weak peak could be observed at 2108 cm^{-1} , corresponding to alkynes $-\text{C}\equiv\text{C}-$.⁵¹ For 1,3,5-triethynyltriphenylbenzene, the stretching vibrational band of phosphonic acid groups $\text{P}=\text{O}$ is located at approximately 940 cm^{-1} . In terms of **CMP-C2-P**, the disappearance of terminal alkynes $-\text{C}\equiv\text{C}-\text{H}$ and $\text{C}-\text{Br}$, the retention of alkynes $-\text{C}\equiv\text{C}-$ (2168 cm^{-1}) and phosphonic acid groups $\text{P}=\text{O}$ (919 cm^{-1}) reveal the success of the coupling reaction. Lastly, the presence of C atoms in various chemical environments in the solid-state ^{13}C cross-polarization magic-angle-spinning (CP/MAS) NMR spectra (Fig. 1a and Fig. S5, ESI[†]) proves the structural integrity of **CMP-Cx-P** and **CMP-P**. Moreover, a scanning electron microscope (SEM) and transmission electron microscope (TEM) were utilized to observe the morphology and nanostructure of **CMP-C2-P** (Fig. 1c and Fig. S6, ESI[†]). SEM images reveal that **CMP-C2-P** possesses a stacked bulk bumpy coral-like morphology within a dimension range of 500 to 3000 nm. TEM images reveal that **CMP-C2-P** exhibits stacked block layered morphology.

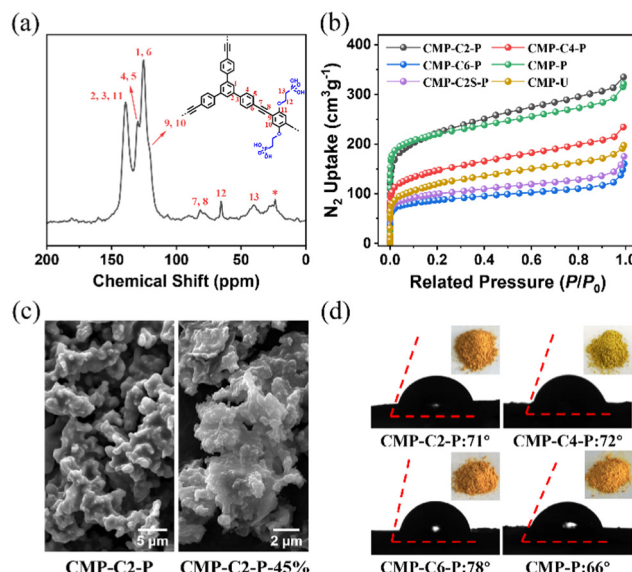


Fig. 1 (a) ^{13}C CP/MAS NMR spectrum of **CMP-C2-P**. Asterisks denote spinning sidebands. (b) N_2 adsorption isotherms of CMPs at 77 K. (c) SEM images of **CMP-C2-P** and **CMP-C2-P-45%**. (d) Water contact angles of **CMP-C2/C4/C6-P** and **CMP-P**.

The thermal stability of **CMPs** was measured by thermogravimetric analysis (TGA) under a nitrogen atmosphere. As shown in Fig. S7 (ESI[†]), **CMP-Cx-P** shows no obvious weight loss before 155°C , which means that the structure has excellent thermal stability until 155°C . And the first weightlessness may be attributed to the partial decomposition of the phosphonic acid groups anchored in the CMPs or the release of free H_2O molecules. In addition, we further heat-treated **CMP-C2-P** at 155°C for 12 h, in which the structural integrity of the heated **CMP-C2-P** is hardly changed as evidenced by the results in the PXRD pattern and FT-IR spectrum (Fig. S8 and S9, ESI[†]). The chemical stability of **CMP-C2-P** in water, 60% HNO_3 , and 40% HCl for 24 hours was tested by FT-IR and N_2 adsorption measurement (Fig. S10–S12, ESI[†]). The unchanged peaks of alkynes $-\text{C}\equiv\text{C}-$ and phosphonic acid groups $\text{P}=\text{O}$ in the FT-IR spectra reveal the steady state of **CMP-C2-P**. The surface area of **CMP-C2-P** soaked in 60% HNO_3 is $563 \text{ m}^2 \text{ g}^{-1}$, demonstrating its good chemical stability in acid as well.

Nitrogen adsorption measurements for **CMPs** were performed at 77 K to explore their porosity. The type-I isotherm curves and sharp absorption at low pressure ($P/P_0 < 0.05$) demonstrates the microporous structure of **CMP-Cx-P**.⁵² The increased N_2 uptake above a partial pressure of 0.2 and the rise in uptake at $P/P_0 > 0.8$ in the isotherm for CMPs may be due to interparticulate porosity associated with the complex meso- and macro-structure of the samples.⁵¹ The Brunauer–Emmett–Teller (BET) surface areas of them are 648, 443, 297, 622, 311, and $421 \text{ m}^2 \text{ g}^{-1}$ for **CMP-C2/C4/C6-P**, **CMP-P**, **CMP-C2S-P** and **CMP-U**, respectively (Fig. 1b). The gradual decrease in surface area of **CMP-Cx-P** is attributed to the different length of the alkoxy phosphonic acid group side chains. Moreover, nonlocal density functional theory (NLDFT) calculation provides the

pore size distribution of **CMPs**, and the pore sizes of **CMP-C2/C4/C6-P**, **CMP-P**, **CMP-C2S-P** and **CMP-U** are centred at 0.79–2.14, 0.99–2.04, 1.11–1.96, 1.40–2.34, 1.11–1.88, and 0.79–2.34 nm, respectively (Fig. S12, ESI[†]). The PXRD data and NLDFT pore size distributions prove that these networks are indeed completely amorphous, consistent with the literature results.⁵¹ Water vapor adsorption measurements were utilized to reveal the water vapor adsorption capacity of CMPs (Fig. S14, ESI[†]). According to the isotherms, the water vapor uptake of **CMP-C2/C4/C6-P** is 47, 47, and 40 cm³ g⁻¹, and the hydrogen-bonding interaction (P=O···H-O) of the oxygen atoms on the wall, promotes the uptake of H₂O molecules.²⁴ Water contact angle measurements further confirm the hydrophilicity for **CMP-Cx-P** (Fig. 1d).

In addition, the electrical conductivity of **CMP-Cx-P** was measured (Fig. S15, ESI[†]). The electronic conductivities of **CMP-C2/C4/C6-P** and **CMP-P** are 8.74×10^{-6} , 8.86×10^{-6} , 6.70×10^{-6} , and 8.28×10^{-6} S m⁻¹, respectively, implying that these CMPs with disordered structures possess poor electrical conductivity.

Characterization of **CMP-Cx-P-H**

The successful anchoring of phosphonic acid groups, high porosity and good thermal stability and acid-resistance of **CMP-Cx-P** enable them to act as anhydrous proton-conducting materials. Afterwards, different qualities of H₃PO₄ were doped into **CMP-Cx-P** by manual grinding. The corresponding CMPs were defined as **CMP-Cx-P-H** (H represents the percentage of doped H₃PO₄ in the total mass). **CMP-Cx-P-H** and **CMP-P-H** show similar PXRD patterns to those of the initial **CMP-Cx-P** and **CMP-P**, implying no change in the structures (Fig. S16, ESI[†]). Besides, the successful doping of H₃PO₄ in the channel of **CMP-Cx-P** is further confirmed by FT-IR spectra, TGA and N₂ adsorption measurements. The FT-IR spectra reveal that alkynes C≡C- and phosphonic acid groups P=O are well maintained (Fig. S17, ESI[†]), and furthermore, the band of P=O (~970 cm⁻¹) became more intense and distinct as the amount of doped H₃PO₄ increases. The BET surface area of **CMP-C2/C4/C6-P-45%**, **CMP-P-45%**, and **CMP-U-45%** sharply reduced to 13, 3, 12, 5, and 7 m² g⁻¹, respectively (Fig. S18 and S19, ESI[†]). Note that after the removal of H₃PO₄, **CMP-C2-P-45%**, shows a BET surface area of 458 m² g⁻¹ (Fig. S12, ESI[†]), which remains above 70% compared with **CMP-C2-P**, showing structural stability in the doping of H₃PO₄. As shown by TGA curves, phosphoric acid, **CMP-C2-P**, and **CMP-C2-P-45%** undergo weight loss at 120, 155, and 140 °C, respectively (Fig. S20, ESI[†]). These results suggest that the pores of **CMP-Cx-P-H** are occupied by guest H₃PO₄ molecules. The introduction of H₃PO₄ leads to a higher water vapor uptake (Fig. S14, ESI[†]), and the uptake of water vapor for **CMP-C2/C4/C6-P-45%** is 425, 384, and 417 cm³ g⁻¹, respectively. This trend corresponds to the water contact angle tests (Fig. 1d and Fig. S21, ESI[†]). After doping with H₃PO₄, SEM and TEM images show that **CMP-C2-P-45%** retains the initial morphology and structure (Fig. 1c and Fig. S6, ESI[†]). These results hint there is no excess H₃PO₄ on the surface of **CMP-C2-P-45%**.

High temperature anhydrous proton conduction

We prepared the cylindrical pellets of these samples with a diameter of 5 mm and a thickness of around 0.4–0.6 mm via pressing the pre-dried CMP powders at a pressure of 0.2 MPa for 30 min under a nitrogen atmosphere, and investigated the proton conductivities over various temperatures from 30 to 130 °C by alternating-current (AC) impedance spectroscopy under anhydrous conditions.

As shown in the Nyquist plots, the resistance values of **CMP-Cx-P-H** and **CMP-P-H** could be directly obtained to calculate the corresponding proton conductivities. To study the proton conductivities of CMPs at various temperatures, we take **CMP-C2-P-H** as an example. **CMP-C2-P** is almost an insulator, exhibiting a high resistance value ($R = \sim 10^8$ Ω) even at 130 °C (Fig. S23, ESI[†]). By comparison, the proton conductivity of **CMP-C2-P-15%** (4.90×10^{-4} S cm⁻¹) is at least 5 orders of magnitude higher than that of **CMP-C2-P** under similar conditions (Fig. S24, ESI[†]). Moreover, **CMP-C2-P-30%/45%/60%** reveals increasingly high proton conductivities of 2.10×10^{-3} , 1.12×10^{-2} , and 2.15×10^{-2} S cm⁻¹ at 130 °C, respectively (Fig. 2a and Fig. S24, ESI[†]). Notably, the proton conductivity of **CMP-C2-P-45%** is nearly 5 times that of our previous reported H₃PO₄@**CMP-F6-45%** (2.83×10^{-3} S cm⁻¹), and is competitive among the reported porous materials (Fig. 2e and Table S1, ESI[†]).^{11,18,25,26,29,30,42,49,53–57} In our previous work, we introduced functional hydrophobic groups into the channel of CMPs to promote anhydrous proton conductivity.⁴² By contrast, in this work, the pre-designed hydrophilic phosphonic acid group anchored CMPs exhibit more efficient anhydrous proton conduction. Furthermore, the activation energies of **CMP-C2-P-15%/30%/45%/60%** obtained within 30–130 °C were 0.73, 0.63, 0.47, and 0.36 eV, respectively (Fig. 2b). Based on these findings, with the increase of doped H₃PO₄, the proton transfer mechanism of **CMP-Cx-P-H** changed from Vehicular mechanisms ($E_a > 0.4$ eV) to Grotthuss mechanisms ($E_a < 0.4$ eV).^{58,59} Hence, due to the remarkable hydrogen-bonding networks formed by the anchored phosphonic acid groups and guest H₃PO₄ molecules, H₂O molecules, we solve the leaching of H₃PO₄ as much as possible, thereby achieving efficient proton hopping.²⁵

Similar to **CMP-C2-P-H**, the proton conductivities of **CMP-C4/C6-P-H** decorated with longer alkoxy side chains were studied. For **CMP-C4/C6-P-45%**, the proton conductivities at 130 °C are 7.76×10^{-3} , and 1.87×10^{-3} S cm⁻¹, respectively. It can be concluded that **CMP-C4/C6-P-H** shows lower proton conductivity compared with **CMP-C2-P-H** (Fig. 2c and Fig. S25, ESI[†]), which is due to longer side chains blocking the size-limited nanopores. Meanwhile, at 130 °C, **CMP-P-45%** ($\sigma = 5.29 \times 10^{-3}$ S cm⁻¹) reveals a lower proton conductivity than those of **CMP-C2/C4-P-45%** and a higher proton conductivity than that of **CMP-C6-P-45%**, which may be due to the lack of flexible alkoxy chains in **CMP-P** structures. Moreover, under the same conditions, the proton conductivity of **CMP-C2S-P-45%** reaches 1.62×10^{-4} S cm⁻¹, while **CMP-U-45%** exhibits the lowest proton conductivity of 9.44×10^{-5} S cm⁻¹ (Fig. 2c and



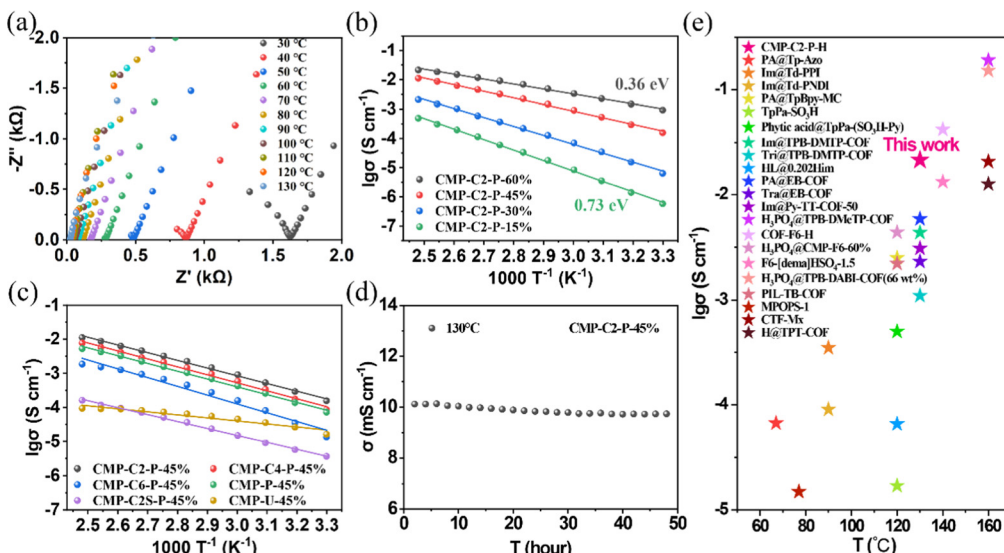


Fig. 2 (a) Nyquist plots for **CMP-C2-P-45%** at 30–130 °C under anhydrous conditions. (b) Arrhenius plots for **CMP-C2-P-H** with a different amount of H_3PO_4 under anhydrous conditions. (c) Arrhenius plots for **CMP-C2/C4/C6-P-45%**, **CMP-P-45%**, **CMP-C2S-P-45%**, and **CMP-U-45%** under anhydrous conditions. (d) Long-period test for **CMP-C2-P-45%** at 130 °C under anhydrous conditions. (e) Comparison of anhydrous proton conductivities in the reported materials.

Fig. S25, ESI ‡), which is nearly 2 orders of magnitude lower than that of **CMP-C2-P-45%**. Therefore, we draw the conclusions that (i) large decorated pores and suitable length of the side chains are both needed to achieve efficient proton conduction; (ii) the bottom-up synthesized hydrophilic phosphonic acid groups anchored in the frameworks contribute significantly to proton transport.

At last, **CMP-C2-P-45%** shows an excellent stability in the long-period test and cycling test. After 48 hours at 130 °C, the proton conductivity of **CMP-C2-P-45%** (9.81×10^{-3} S cm $^{-1}$) only decreased by 6.2% per day, and the value tended to be constant after 20 hours (Fig. 2d). The proton transport capability of the second cycling test is consistent with the initial test (Fig. S26, ESI ‡). These results indicate the excellent thermal and electrochemical stability of **CMP-C x -P-H**, confirming that guest H_3PO_4 molecules are anchored inside the structure. Elevating the temperature above 140 °C may cause a decrease in proton conductivity, which is due to the partial decomposition of H_3PO_4 molecules (Fig. S20, ESI ‡).

Subzero temperature anhydrous proton conduction

Inspired by the high anhydrous proton conductivities of **CMP-C2-P-60%** from room temperature to 130 °C (9.29×10^{-4} and 2.15×10^{-2} S cm $^{-1}$ at 30 and 130 °C, respectively) and the solid hydrogen-bonding networks, we further measured the proton conductivity of **CMP-C x -P-H** and **CMP-P-H** within a low temperature range from –40 to 0 °C. The anhydrous proton conductivity of **CMP-C2-P-60%** at –40 °C is 1.15×10^{-5} S cm $^{-1}$, and the activation energy over the temperature range of –40 to 0 °C is 0.55 eV (Fig. 3a and b), which demonstrates a good proton transport efficiency compared to other porous materials (Fig. 3d and Table S1, ESI ‡). Note that in the plot of $\ln(\sigma T)$ against $1000 T^{-1}$ between –40 and 130 °C, **CMP-C2-P-60%** exhibits a

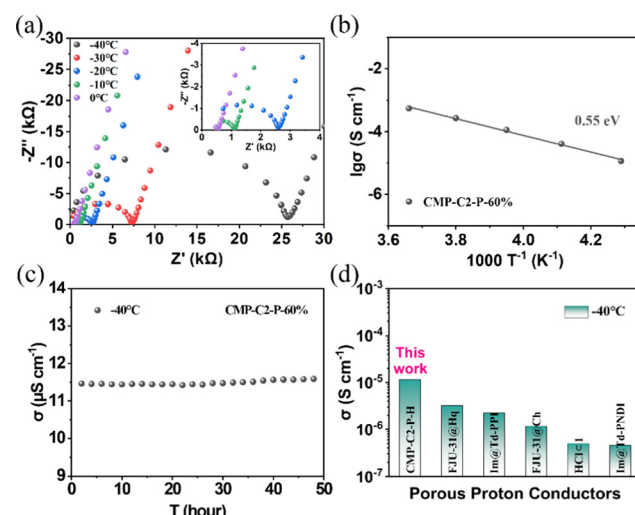


Fig. 3 (a) Nyquist plots for **CMP-C2-P-60%** at –40 to 0 °C under anhydrous conditions. (b) Arrhenius plots for **CMP-C2-P-60%** under anhydrous conditions. (c) Long-period test for **CMP-C2-P-60%** at –40 °C under anhydrous conditions. (d) Comparison of anhydrous proton conductivities in the reported materials measured at –40 °C.

nonlinear relationship across the entire temperature range (Fig. S27, ESI ‡). This can be attributed to a weak structural change which was commonly observed in similar porous materials.^{57,60–63} Additionally, **CMP-C2/C4/C6-P-45%** and **CMP-P-45%** obtain proton conductivities of 2.33×10^{-7} , 9.61×10^{-8} , 1.04×10^{-8} , and 2.68×10^{-8} S cm $^{-1}$ at –40 °C, respectively (Fig. S28, ESI ‡). For comparison, $\text{H}_3\text{PO}_4@\text{CMP-F6-45\%}$ was also measured under the same conditions (Fig. S29, ESI ‡). The proton conductivity of $\text{H}_3\text{PO}_4@\text{CMP-F6-45\%}$ ($\sim 10^{-10}$ S cm $^{-1}$) is 3 orders of magnitude lower than that of **CMP-C2-P-45%**. This result is possibly due to

the strong $\text{P}=\text{O}\cdots\text{H}-\text{O}$ hydrogen-bonds formed inside **CMP-Cx-P-H**, which makes the hydrogen-bonding network system more stable within the structure. In particular, **CMP-C2-P-60%** also performs very well in the long-period test (Fig. 3c). In conclusion, **CMP-Cx-P-H** can be applied within a wide temperature range, subzero temperature—room temperature—high temperature.

Humid proton conduction

Considering the hydrophilic phosphonic acid groups anchored in the pores of **CMP-Cx-P**, we further measured the proton conductances of **CMP-C2-P** and **CMP-C2-P-H** under humidity conditions. Cylindrical pellets of **CMP-C2-P** and **CMP-C2-P-H** with a diameter of 5 mm and a thickness of around 0.5–0.7 mm were prepared. The pellets were sealed in a glass bottle with a certain relative humidity, and were then measured from 30 to 90 °C.

As given by Nyquist plots, **CMP-C2-P** possesses the proton conductivities of 8.95×10^{-9} , 2.77×10^{-7} , and 2.17×10^{-5} S cm $^{-1}$ under 32%, 56%, and 84% RH at 30 °C, respectively (Fig. 4b and Fig. S30, ESI \dagger). In contrast, **CMP-C2-P-45%** exhibits proton conductivities of 1.87×10^{-2} , 3.28×10^{-2} , and 4.86×10^{-2} S cm $^{-1}$ under 32%, 56%, and 84% RH at 30 °C, respectively (Fig. 4b and Fig. S31, ESI \dagger). Furthermore, at different temperatures, the proton conductivities of **CMP-C2-P** are obtained under 98% RH (1.84×10^{-4} , 7.59×10^{-4} , and 9.89×10^{-3} S cm $^{-1}$ at 30, 60, and 90 °C, respectively) (Fig. S32, ESI \dagger). Ulteriorly, under 98% RH, the proton conductivities of **CMP-C2-P-45%** are 5.87×10^{-2} , 7.99×10^{-2} , and 9.93×10^{-2} S cm $^{-1}$ at 30, 60 and 90 °C, respectively (Fig. 4a). It is worth mentioning that (i) **CMP-C2-P** was capable of possessing a relatively high intrinsic proton conductivity after adsorbing water. Although **CMP-C2-P** obtains negligible anhydrous proton conductivity, the proton conductivity value increases prominently under humid conditions; (ii) the humid proton conductivity of

CMP-C2-45% under 98% RH at 90 °C is 31 times the anhydrous proton conductivity of **CMP-C2-45%** (3.23×10^{-3} S cm $^{-1}$ at 90 °C). These observations illustrates that (i) the hydration of the CMPs under high humidity is of importance for proton conduction of these non-intrinsic proton-conducting materials;^{24,64} (ii) the obvious superiority of **CMP-Cx-P-H** over the initial **CMP-Cx-P** can be attributed to the dense hydrogen-bonding networks involving both H_3PO_4 and H_2O molecules that are formed and fixed within the nanostructure.²⁴ In the temperature range of 30–90 °C, the activation energies for the proton transport in **CMP-C2-P** and **CMP-C2-P-45%** are 0.65 and 0.11 eV, respectively (Fig. 4c), implying a relatively low energy barrier and easier transfer of proton carriers in **CMP-Cx-P-H**.

We measured the samples of H_3PO_4 @**CMP-F6-45%** under 98% RH as well (Fig. S33 and S34, ESI \dagger). The proton conductivity of 5.51×10^{-3} S cm $^{-1}$ obtained for H_3PO_4 @**CMP-F6-45%** at 90 °C is 1 order of magnitude lower than **CMP-C2-P-45%** ($\sigma = 9.93 \times 10^{-2}$ S cm $^{-1}$), which was attributed to the significant difference in hydrophilicity and hydrophobicity. According to the water contact angle tests (Fig. 1d and Fig. S22, ESI \dagger), on account of the pre-design multiple hydrophilic groups, phosphonic acid groups, **CMP-Cx-P** and **CMP-P** show certain hydrophilicities (71° , 72° , 78° , and 66° for **CMP-C2/C4/C6-P** and **CMP-P**, respectively). After further doping with H_3PO_4 , **CMP-Cx-P-H** and **CMP-P** exhibit superhydrophilicity (19° , 30° , 34° , and 17° for **CMP-C2/C4/C6-45%** and **CMP-P-45%**, respectively). Apparently, the more pronounced property in hydrophilicity of **CMP-C2-P-45%** than that of the previously reported H_3PO_4 @**CMP-F6-45%** and notable water vapor uptake mean a better adsorption capacity for H_2O molecules, which is essential to humid proton conductivity.

Furthermore, a long-period test for **CMP-C2-P-45%** was also performed under 98% RH at different temperatures (Fig. 4d and Fig. S35, ESI \dagger), in which, at 30 and 70 °C, **CMP-C2-P-45%**

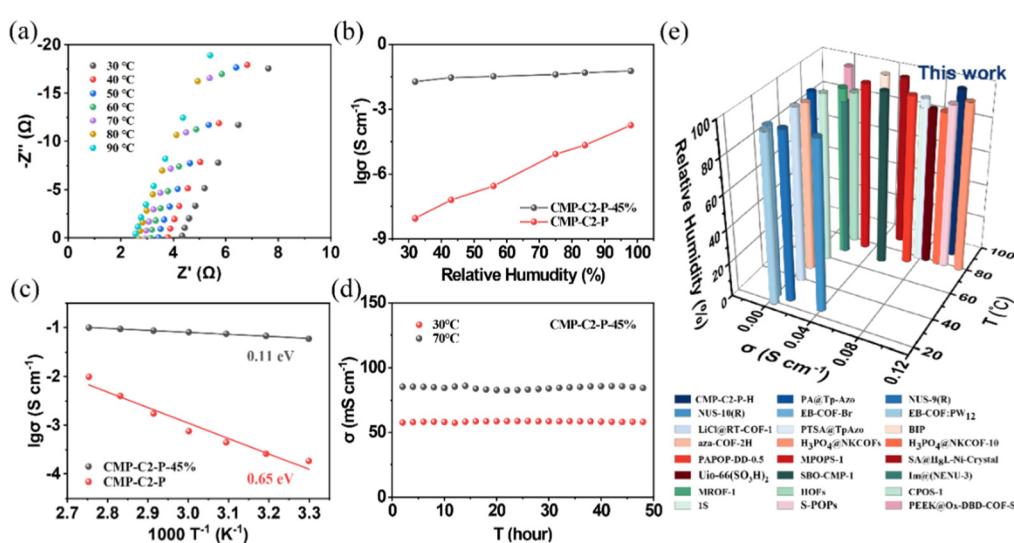


Fig. 4 (a) Nyquist plots of **CMP-C2-P-45%** under 98% RH at 30–90 °C. (b) Proton conductivities for **CMP-C2-P** and **CMP-C2-P-45%** under different relative humidities at 30 °C. (c) Arrhenius plots for **CMP-C2-P** and **CMP-C2-P-45%** under 98% RH. (d) Long-period test for **CMP-C2-P-45%** under 98% RH at 70 °C. (e) Comparison of humid proton conductivities in reported materials.



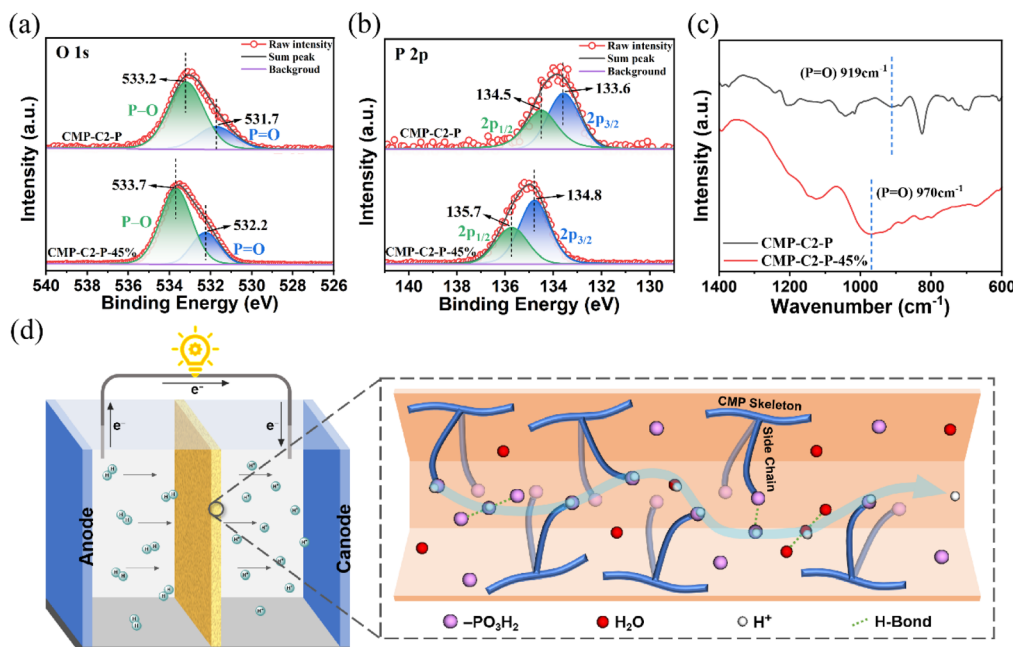


Fig. 5 XPS spectra of (a) O1s bands of **CMP-C2-P** and **CMP-C2-P-45%**, and (b) P2p bands of **CMP-C2-P** and **CMP-C2-P-45%**. (c) FT-IR spectra of **CMP-C2-P** and **CMP-C2-P-45%**. (d) Illustration for the proposed humid proton conduction mechanism of **CMP-Cx-P-H**.

displays high and persistent proton conductivities of about 5.84×10^{-2} and 8.46×10^{-2} S cm⁻¹ for more than 48 hours, respectively. However, at 90 °C, it shows an average proton conductivity of 7.09×10^{-2} S cm⁻¹ within 48 h, which was 22.1% lower than the initial value. As for the proton conductivity degradation caused by a further increase in temperature above 70 °C, it is attributed to the loss of H₃PO₄ molecules when the operating temperature is too high. Notably, **CMP-C2-P-H** exhibits a good proton transfer capability among other porous materials reported in the literature (Fig. 4e and Table S1, ESI[†]).^{23,24,27,28,30,41,43–45,49,64–75} According to this result, **CMP-Cx-P-H** performs well with an excellent electrochemical stability under humid conditions. In the meantime, it demonstrates that **CMP-Cx-P-H** not only shows high efficiency and stability in anhydrous proton conduction, but is also promising for application in proton conduction under relative humidity.

Involving the doped guest H₃PO₄ molecules, the abundant P=O and O-H groups on the nanopore walls of **CMP-Cx-P** show potential sites of hydrogen bonds (Scheme 1b). The interactions between **CMP-Cx-P** and the doped guest H₃PO₄ molecules are illustrated by X-ray photoelectron spectroscopy (XPS). The high-resolution O1s spectra of **CMP-C2-P** are shown in Fig. 5a. Two peaks appear at 531.7 and 533.2 eV, which are assigned to the O atoms of P=O and P-O bonds, respectively.⁷⁶ The high-resolution O1s spectra (Fig. 5a) of **CMP-C2-P-45%** show two peaks at 532.2 and 533.7 eV, indicating that the effective binding energy values of the O atoms of the P=O/P-O bonds significantly increase due to the interactions between the anchored phosphonic acid groups in the **CMP-C2-P** structure and guest H₃PO₄ molecules. The P 2p_{3/2}/P 2p_{1/2} doublet is fitted

with an energy difference of 0.9 eV in **CMP-C2-P** and **CMP-C2-P-45%** (Fig. 5b).⁷⁷ Besides, BE = 133.6 eV (P 2p_{3/2}) and BE = 134.5 eV (P 2p_{1/2}) change to 134.8 and 135.7 eV, respectively, reflecting the existence of P=O···H-O hydrogen-bonds. In addition, a shift of 51 cm⁻¹ for the stretching vibrational band of the P=O bond from 919 cm⁻¹ of **CMP-C2-P** to 970 cm⁻¹ of **CMP-C2-P-45%** in the FT-IR spectra (Fig. 5c) indicates the formation of P=O···H-O hydrogen-bonds as well.^{55,78,79} As shown in Fig. 5d, the disordered structure of **CMP-Cx-P-H** provides stable and in-all-directions channels for proton transport under humid conditions. The abundance of phosphonic acid groups can act as a support and a proton donor, and provide sites for anchoring the H₃PO₄ network through hydrogen-bonding of P=O···H-O. Based on the experimental facts of **CMP-C2-P-45%**, we believe that some of the H₃PO₄ molecules are anchored in the pore walls, while most H₃PO₄ molecules and H₂O molecules are linked together and form proton-conducting channels by hydrogen-bonding. Furthermore, alkoxy side chains and H₃PO₄ molecules are highly dynamic and mobile and integrating with the hydrophilic side chains and the hydrophobic skeleton promotes the microphase separation inside the CMPs, thus side chains prompt phosphonic acid groups to move close to H₂O molecules and form hydrated protons, and by the rotation of H₃PO₄ molecules, protons can hop across the hydrogen-bonding networks, promoting the mobility of protons.^{26,80,81}

Conclusions

In summary, the universal proton-conducting materials—the phosphonic acid group-functionalized CMPs, **CMP-Cx-P-H**, are



demonstrated for the first time by a bottom-up strategy with side-chain engineering. The multiple phosphonic acid side chains that are highly dynamic and anchored within the channels are helpful to form a hydrophilic environment and dense hydrogen bonds with the guest H_3PO_4 molecules. With the strong hydrogen-bonding networks, **CMP-C2-P-H** showed excellent proton conductivities under various conditions, including 2.15×10^{-2} and $1.15 \times 10^{-5} \text{ S cm}^{-1}$ at 130 and -40°C , respectively, under anhydrous conditions, as well as $9.93 \times 10^{-2} \text{ S cm}^{-1}$ at 90°C under 98% relative humidity. **CMP-Cx-P-H** are the first porous organic polymer proton-conducting materials proposed to be suitable for both humid and anhydrous dual scenarios, as well as being universal over an ultra-wide temperature range of -40°C to 130°C . This work paves the way for realizing multi-environmental applications of polymer electrolyte membrane fuel cells and their use in extreme conditions.

Author contributions

Kaijie Yang: synthesis, methodology, validation, investigation, data curation, and writing. Yuxiang Wang: investigation, data curation, and formal analysis. Zhiyi Ling: investigation, data curation, and formal analysis. Xiaogang Pan: investigation. Gen Zhang: validation, and writing – review & editing. Jian Su: validation, and writing – review & editing.

Conflicts of interest

There are no conflicts to declare.

Acknowledgements

The authors are grateful to Prof. Jing-Lin Zuo at Nanjing University for his help in this work. This work was financially supported by startup funding from the Nanjing University of Science and Technology (AE89991/194, AE89991/259, AD41913, AD41960, and AE89991/376), the National Natural Science Foundation of China (22171136), “the Fundamental Research Funds for the Central Universities” (30921011102, 30922010301, 30922010902), and the Natural Science Foundation of Jiangsu Province (BK20220079, BK20220928). G. Z. acknowledges the support from the Thousand Young Talent Plans.

References

- 1 K. A. Mauritz and R. B. Moore, *Chem. Rev.*, 2004, **104**, 4535–4585.
- 2 K. Schmidt-Rohr and Q. Chen, *Nat. Mater.*, 2008, **7**, 75–83.
- 3 R. Devanathan, *Energy Environ. Sci.*, 2008, **1**, 101–119.
- 4 G. L. Jackson, D. V. Perroni and M. K. Mahanthappa, *J. Phys. Chem. B*, 2017, **121**, 9429–9436.
- 5 S. J. Paddison, *Annu. Rev. Mater. Res.*, 2003, **33**, 289–319.
- 6 Y. Wang, K. S. Chen, J. Mishler, S. C. Cho and X. C. Adroher, *Appl. Energy*, 2011, **88**, 981–1007.
- 7 R. K. Ahluwalia, X. Wang, W. B. Johnson, F. Berg and D. Kadylak, *J. Power Sources*, 2015, **291**, 225–238.
- 8 Y. Yin, Z. Li, X. Yang, L. Cao, C. Wang, B. Zhang, H. Wu and Z. Jiang, *J. Power Sources*, 2016, **332**, 265–273.
- 9 E. Quartarone and P. Mustarelli, *Energy Environ. Sci.*, 2012, **5**, 6436–6444.
- 10 S. Y. Kim, S. Kim and M. J. Park, *Nat. Commun.*, 2010, **1**, 88.
- 11 Y. X. Ye, L. Q. Zhang, Q. F. Peng, G. E. Wang, Y. C. Shen, Z. Y. Li, L. H. Wang, X. L. Ma, Q. H. Chen, Z. J. Zhang and S. C. Xiang, *J. Am. Chem. Soc.*, 2015, **137**, 913–918.
- 12 D. W. Shin, M. D. Guiver and Y. M. Lee, *Chem. Rev.*, 2017, **117**, 4759–4805.
- 13 Y. Chen, M. Thorn, S. Christensen, C. Versek, A. Poe, R. C. Hayward, M. T. Tuominen and S. Thayumanavan, *Nat. Chem.*, 2010, **2**, 503–508.
- 14 L. Vilcinskas, M. E. Tuckerman, G. Bester, S. J. Paddison and K.-D. Kreuer, *Nat. Chem.*, 2012, **4**, 461–466.
- 15 S.-Y. Moon, J.-S. Bae, E. Jeon and J.-W. Park, *Angew. Chem., Int. Ed.*, 2010, **49**, 9504–9508.
- 16 W. Luo, Y. Zhu, J. Zhang, J. He, Z. Chi, P. W. Miller, L. Chen and C.-Y. Su, *Chem. Commun.*, 2014, **50**, 11942–11945.
- 17 Y. Wang, D. F. R. Diaz, K. S. Chen, Z. Wang and X. C. Adroher, *Mater. Today*, 2020, **32**, 178–203.
- 18 D. B. Shinde, H. B. Aiyappa, M. Bhadra, B. P. Biswal, P. Wadge, S. Kandambeth, B. Garai, T. Kundu, S. Kurungot and R. Banerjee, *J. Mater. Chem. A*, 2016, **4**, 2682–2690.
- 19 R. S. Raja Rafidah, W. Rashmi, M. Khalid, W. Y. Wong and J. Priyanka, *Polymers*, 2020, **12**, 1061.
- 20 S. C. Sahoo, T. Kundu and R. Banerjee, *J. Am. Chem. Soc.*, 2011, **133**, 17950–17958.
- 21 F. Yang, G. Xu, Y. Dou, B. Wang, H. Zhang, H. Wu, W. Zhou, J.-R. Li and B. Chen, *Nat. Energy*, 2017, **2**, 877–883.
- 22 M. Yoon, K. Suh, S. Natarajan and K. Kim, *Angew. Chem., Int. Ed.*, 2013, **52**, 2688–2700.
- 23 D. Chakraborty, A. Ghorai, A. Chowdhury, S. Banerjee and A. Bhaumik, *Chem. – Asian J.*, 2021, **16**, 1562–1569.
- 24 Z. Meng, A. Aykanat and K. A. Mirica, *Chem. Mater.*, 2019, **31**, 819–825.
- 25 S. Tao, L. Zhai, A. D. Dinga Wonanke, M. A. Addicoat, Q. Jiang and D. Jiang, *Nat. Commun.*, 2020, **11**, 1981.
- 26 X. Wu, Y.-l Hong, B. Xu, Y. Nishiyama, W. Jiang, J. Zhu, G. Zhang, S. Kitagawa and S. Horike, *J. Am. Chem. Soc.*, 2020, **142**, 14357–14364.
- 27 D. W. Kang, J. H. Song, K. J. Lee, H. G. Lee, J. E. Kim, H. Y. Lee, J. Y. Kim and C. S. Hong, *J. Mater. Chem. A*, 2017, **5**, 17492–17498.
- 28 D. W. Kang, K. S. Lim, K. J. Lee, J. H. Lee, W. R. Lee, J. H. Song, K. H. Yeom, J. Y. Kim and C. S. Hong, *Angew. Chem., Int. Ed.*, 2016, **55**, 16123–16126.
- 29 A. Jankowska, A. Zalewska, A. Skalska, A. Ostrowski and S. Kowalak, *Chem. Commun.*, 2017, **53**, 2475–2478.
- 30 P. Bhanja, A. Paui, S. Chatterjee, Y. V. Kaneti, J. Na, Y. Sugahara, A. Bhaumik and Y. Yamauchi, *ACS Sustainable Chem. Eng.*, 2020, **8**, 2423–2432.
- 31 A. Modak, M. Nandi, J. Mondal and A. Bhaumik, *Chem. Commun.*, 2012, **48**, 248–250.



32 P. Lindemann, M. Tsotsalas, S. Shishatskiy, V. Abetz, P. Krolla-Sidenstein, C. Azucena, L. Monnereau, A. Beyer, A. Goelzhaeuser, V. Mugnaini, H. Gliemann, S. Braese and C. Woell, *Chem. Mater.*, 2014, **26**, 7189–7193.

33 K. V. Rao, S. Mohapatra, T. K. Maji and S. J. George, *Chem. – Eur. J.*, 2012, **18**, 4505–4509.

34 X.-S. Wang, J. Liu, J. M. Bonefont, D.-Q. Yuan, P. K. Thallapally and S. Ma, *Chem. Commun.*, 2013, **49**, 1533–1535.

35 A. Modak, J. Mondal and A. Bhaumik, *Appl. Catal. A-Gen.*, 2013, **459**, 41–51.

36 H. Zhao, G. Yu, M. Yuan, J. Yang, D. Xu and Z. Dong, *Nanoscale*, 2018, **10**, 21466–21474.

37 N. Kang, J. H. Park, K. C. Ko, J. Chun, E. Kim, H.-W. Shin, S. M. Lee, H. J. Kim, T. K. Ahn, J. Y. Lee and S. U. Son, *Angew. Chem., Int. Ed.*, 2013, **52**, 6228–6232.

38 Z. J. Wang, S. Ghasimi, K. Landfester and K. A. I. Zhang, *Chem. Commun.*, 2014, **50**, 8177–8180.

39 Y. Xu, A. Nagai and D. Jiang, *Chem. Commun.*, 2013, **49**, 1591–1593.

40 P. Zhang, K. Wu, J. Guo and C. Wang, *ACS Macro Lett.*, 2014, **3**, 1139–1144.

41 S.-J. Yang, X. Ding and B.-H. Han, *Langmuir*, 2018, **34**, 7640–7646.

42 X. Jiang, K. Zhang, Y. Huang, B. Xu, X. Xu, J. Zhang, Z. Liu, Y. Wang, Y. Pan, S. Bian, Q. Chen, X. Wu and G. Zhang, *ACS Appl. Mater. Interfaces*, 2021, **13**, 15536–15541.

43 Z. Li, Y. Yao, D. Wang, M. M. Hasan, A. Suwansoontorn, H. Li, G. Du, Z. Liu and Y. Nagao, *Mat. Chem. Front.*, 2020, **4**, 2339–2345.

44 C. Klumpen, S. Goedrich, G. Papastavrou and J. Senker, *Chem. Commun.*, 2017, **53**, 7592–7595.

45 T. Zhu, B. Shi, H. Wu, X. You, X. Wang, C. Fan, Q. Peng and Z. Jiang, *Ind. Eng. Chem. Res.*, 2021, **60**, 6337–6343.

46 P. Li, J. Chen and S. Tang, *Chem. Eng. J.*, 2021, **415**, 129021.

47 C. Fan, H. Wu, Y. Li, B. Shi, X. He, M. Qiu, X. Mao and Z. Jiang, *Solid State Ionics*, 2020, **349**, 115316.

48 B. Zhou, J. Le, Z. Cheng, X. Zhao, M. Shen, M. Xie, B. Hu, X. Yang, L. Chen and H. Chen, *ACS Appl. Mater. Interfaces*, 2020, **12**, 8198–8205.

49 S. Chandra, T. Kundu, S. Kandambeth, R. BabaRao, Y. Marathe, S. M. Kunjir and R. Banerjee, *J. Am. Chem. Soc.*, 2014, **136**, 6570–6573.

50 D. Gui, W. Duan, J. Shu, F. Zhai and S. Wang, *CCS Chem.*, 2019, **1**, 197–206.

51 J.-X. Jiang, F. Su, A. Trewin, C. D. Wood, N. L. Campbell, H. Niu, C. Dickinson, A. Y. Ganin, M. J. Rosseinsky, Y. Z. Khimyak and A. I. Cooper, *Angew. Chem., Int. Ed.*, 2007, **46**, 8574–8578.

52 K. S. W. Sing, *Pure Appl. Chem.*, 1985, **57**, 603–619.

53 H. Xu, S. Tao and D. Jiang, *Nat. Mater.*, 2016, **15**, 722.

54 S. Chandra, T. Kundu, K. Dey, M. Addicoat, T. Heine and R. Banerjee, *Chem. Mater.*, 2016, **28**, 1489–1494.

55 J. Li, J. Wang, Z. Wu, S. Tao and D. Jiang, *Angew. Chem., Int. Ed.*, 2021, **60**, 12918–12923.

56 Y. Guo, X. Zou, W. Li, Y. Hu, Z. Jin, Z. Sun, S. Gong, S. Guo and F. Yan, *J. Mater. Chem. A*, 2022, **10**, 6499–6507.

57 W. Huang, B. Li, Y. Wu, Y. Zhang, W. Zhang, S. Chen, Y. Fu, T. Yan and H. Ma, *ACS Appl. Mater. Interfaces*, 2021, **13**, 13604–13612.

58 P. Ramaswamy, N. E. Wong and G. K. H. Shimizu, *Chem. Soc. Rev.*, 2014, **43**, 5913–5932.

59 S. Pili, S. P. Argent, C. G. Morris, P. Rought, V. Garcia-Sakai, I. P. Silverwood, T. L. Easun, M. Li, M. R. Warren, C. A. Murray, C. C. Tang, S. Yang and M. Schroeder, *J. Am. Chem. Soc.*, 2016, **138**, 6352–6355.

60 H.-B. Luo, L.-T. Ren, W.-H. Ning, S.-X. Liu, J.-L. Liu and X.-M. Ren, *Adv. Mater.*, 2016, **28**, 1663–1667.

61 Y. Ye, X. Wu, Z. Yao, L. Wu, Z. Cai, L. Wang, X. Ma, Q.-H. Chen, Z. Zhang and S. Xiang, *J. Mater. Chem. A*, 2016, **4**, 4062–4070.

62 J. A. Hurd, R. Vaidhyanathan, V. Thangadurai, C. I. Ratcliffe, I. L. Moudrakovski and G. K. H. Shimizu, *Nat. Chem.*, 2009, **1**, 705–710.

63 B. Hou, S. Yang, B. Li, G. Li, H. Zheng, C. Qin, G. Shan, Z. Su and X. Wang, *Inorg. Chem. Front.*, 2022, **9**, 4376–4384.

64 Z. Wang, Y. Yang, Z. Zhao, P. Zhang, Y. Zhang, J. Liu, S. Ma, P. Cheng, Y. Chen and Z. Zhang, *Nat. Commun.*, 2021, **12**, 1982.

65 Y. W. Peng, G. D. Xu, Z. G. Hu, Y. D. Cheng, C. L. Chi, D. Q. Yuan, H. S. Cheng and D. Zhao, *ACS Appl. Mater. Interfaces*, 2016, **8**, 18505–18512.

66 H. P. Ma, B. L. Liu, B. Li, L. M. Zhang, Y. G. Li, H. Q. Tan, H. Y. Zang and G. S. Zhu, *J. Am. Chem. Soc.*, 2016, **138**, 5897–5903.

67 C. Montoro, D. Rodriguez-San-Miguel, E. Polo, R. Escudero-Cid, M. L. Ruiz-Gonzalez, J. A. R. Navarro, P. Ocon and F. Zamora, *J. Am. Chem. Soc.*, 2017, **139**, 10079–10086.

68 H. S. Sasmal, H. B. Aiyappa, S. N. Bhange, S. Karak, A. Halder, S. Kurungot and R. Banerjee, *Angew. Chem., Int. Ed.*, 2018, **57**, 10894–10898.

69 K. C. Ranjeesh, R. Ilathvalappil, S. D. Veer, J. Peter, V. C. Wakchaure, Goudappagouda, K. V. Raj, S. Kurungot and S. S. Babu, *J. Am. Chem. Soc.*, 2019, **141**, 14950–14954.

70 Y. Yang, X. He, P. Zhang, Y. H. Andaloussi, H. Zhang, Z. Jiang, Y. Chen, S. Ma, P. Cheng and Z. Zhang, *Angew. Chem., Int. Ed.*, 2020, **59**, 3678–3684.

71 Z. Yang, P. Chen, W. Hao, Z. Xie, Y. Feng, G. Xing and L. Chen, *Chem. – Eur. J.*, 2021, **27**, 3817–3822.

72 W. J. Phang, H. Jo, W. R. Lee, J. H. Song, K. Yoo, B. Kim and C. S. Hong, *Angew. Chem., Int. Ed.*, 2015, **54**, 5142–5146.

73 Y. Ye, W. Guo, L. Wan, Z. Li, Z. Song, J. Chen, Z. Zhang, S. Xiang and B. Chen, *J. Am. Chem. Soc.*, 2017, **139**, 15604–15607.

74 Y.-H. Han, Y. Ye, C. Tian, Z. Zhang, S.-W. Du and S. Xiang, *J. Mater. Chem. A*, 2016, **4**, 18742–18746.

75 D. W. Kang, M. Kang and C. S. Hong, *J. Mater. Chem. A*, 2020, **8**, 7474–7494.

76 P. Y. Shih, S. W. Yung and T. S. Chin, *J. Non-Cryst. Solids*, 1999, **244**, 211–222.

77 A. Majjane, A. Chahine, M. Et-tabirou, B. Echchahed, D. Trong-On and P. Mc Breen, *Mater. Chem. Phys.*, 2014, **143**, 779–787.



78 M. Textor, L. Ruiz, R. Hofer, A. Rossi, K. Feldman, G. Hahner and N. D. Spencer, *Langmuir*, 2000, **16**, 3257–3271.

79 X. Chen, M. Addicoat, E. Jin, L. Zhai, H. Xu, N. Huang, Z. Guo, L. Liu, S. Irle and D. Jiang, *J. Am. Chem. Soc.*, 2015, **137**, 3241–3247.

80 Z. Lu, C. Yang, L. He, J. Hong, C. Huang, T. Wu, X. Wang, Z. Wu, X. Liu, Z. Miao, B. Zeng, Y. Xu, C. Yuan and L. Dai, *J. Am. Chem. Soc.*, 2022, **144**, 9624–9633.

81 S. Wang, X. Tang, K. Yang, B. Chen, K. Zhang, H. Xu, W. Wang, G. Zhang and C. Gu, *Macromol. Rapid Commun.*, 2022, e2200678.

